Editors' Suggestion

Control of Chemical Waves by Fluid Stretching and Compression

S. Izumoto,[1] D. M. Escala,[1] J. Heyman,[2] T. Le Borgne,[2] and A. De Wit[1]
[1]Nonlinear Physical Chemistry Unit, CP231 Université libre de Bruxelles (ULB), 1050 Brussels, Belgium
[2]Géosciences Rennes, Université de Rennes, UMR CNRS 6118, 263 Avenue du Général Leclerc, F-35042 Rennes, France

(Received 26 March 2024; accepted 16 October 2024; published 21 November 2024)

Oscillatory kinetics coupled to diffusion can produce traveling waves as observed in physical, chemical, and biological systems. We show experimentally that the properties of such waves can be controlled by fluid stretching and compression in a hyperbolic flow. Localized packet waves consisting in a train of parallel waves can develop due to a balance between diffusive broadening and advective compression along the unstable manifold. At a given distance from the stagnation point, the parallel waves transform into planelike waves and smeared waves where the transverse parabolic flow profile disturbs the patterns in the gap width. Once a wave packet has been obtained, it imprints a privileged direction that is maintained even if the compression rate is decreased. The width of the wave packet then scales inversely with the compression rate.

DOI: 10.1103/PhysRevLett.133.218001

Chemical waves, i.e., concentration modulations propagating in a reaction-diffusion (RD) system, are typical spatio-temporal self-organized structures observed in chemical [1–3] and biological systems [4–6]. In an excitable regime, waves also have applications in neuronal dynamics [7] or electrical activity of the heart [8–10], for instance. Their direction, wavelength, and frequency may encode functional information; hence, there is a broad interest in being able to control them [11–13]. In that respect, strategies to target specific wave dynamics have been devised using systems as diverse as DNA-based chemical reaction networks [14], light-sensitive media [15,16], or complex geometries [17], to name a few. In parallel, several studies have also demonstrated the influence of advective transport on wave formation [18–21]. In particular, complex wave dynamics under advection have been observed, for instance, in cellular flows [22–26] and Faraday waves [27]. Active interplay between oscillating reactions and convective instabilities have also demonstrated how chemohydrodynamic interplay can modify the properties of waves [28,29].

Localized oscillatory regions and wave packets have been observed under some conditions in oscillating RD systems in absence of flow [30–33]. Such wave packets extend the potential for applications such as sending and storing directional and quantitative information. Here we investigate how RD waves can be controlled by fluid stretching and compression. To do so, we consider hyperbolic flows, which are characterized by constant stretching and compression. They are a model system for a wide variety of natural flows with stagnation points and perpendicular stable and unstable manifolds that serve as transport barriers [34]. In the vicinity of the stagnation point, fluid elements experience exponential compression and elongation enhancing mixing and the yield of chemical reactions [35–38]. Specifically, we show experimentally that injecting solutions of an oscillating reaction in a hyperbolic flow generates a localized wave packet, i.e., a zone of finite and constant width in which aligned plane waves propagate. We show how the properties of the wave packet can be controlled by the compression rate in the fluid flow.

The reactive solution is an aqueous solution of the bubble-free Belousov-Zhabotinsky-1,4-cyclohexanedione (hereafter BZ-CHD) oscillating reaction with concentrations $[NaBrO_3] = 0.0850$ M, $[NaBr] = 0.0285$ M, [Ferroin] = 0.4 mM, [1,4-cyclohexanedione] = 0.18 M, $[Na_2SO_4] = 0.0750$ M, and $[H_2SO_4] = 2.54$ M [28,39,40]. These specific concentrations were chosen to induce chemical waves with frequency and wavelength compatible with our experimental setup. The latter consists in a reactor made of two 110 mm × 110 mm plates of polymethyl methacrylate (PMMA) separated by a thin gap of 0.5 mm. To create a hyperbolic flow with constant stretching and compression rates, the inner boundaries of the reactor are shaped following the equation $y = \pm 100/x$ (in mm scale) with a pair of inlet and outlet ports positioned at opposite branches of the cell [Fig. 1(a)]. The reactive BZ-CHD solution is injected at a given flow rate Q from both inlets. The velocity $\vec{v} = (v_x, v_y)$ in the cell is given by $v_x = \gamma x$, $v_y = -\gamma y$, where x and y are, respectively, the horizontal unstable and the vertical stable manifold directions and γ is the compression rate, which is the control parameter of the mixing problem [41]. Except in the vicinity of the boundaries, γ is constant everywhere in the cell and equal to $\gamma = \partial v_x/\partial x = Q/Al$ (s^{-1}), where A is the area of the inlet and l is half the distance between the injection points [see Fig. 1(a) and Supplemental Material (SM), Sec. I, for details on the experimental setup [42]].

In the absence of flow ($\gamma = 0$), the BZ-CHD RD system features spatiotemporal traveling target patterns produced

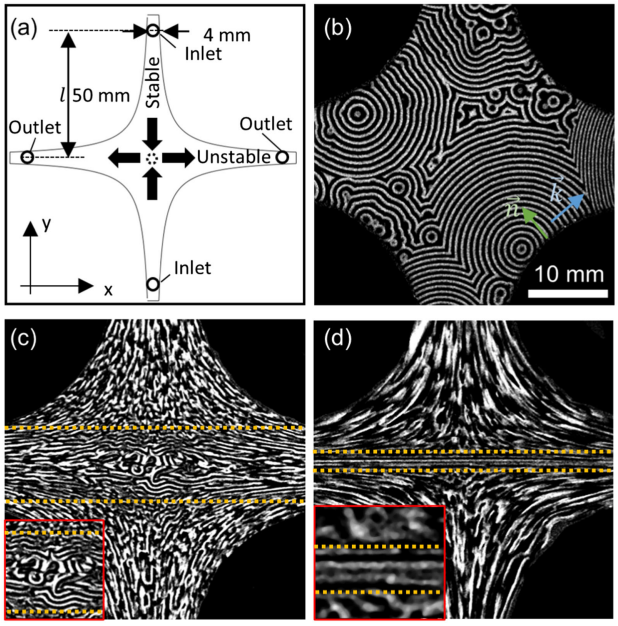

FIG. 1. (a) Schematics of the experimental setup. Two pairs of inlet and outlet holes of 4 mm in diameter are fit to the channel size. The dotted circle in the geometric center of the cell indicates the position of the stagnation point. The inlets and outlets are separated by 50 mm from the stagnation point. The arrows indicate the flow direction. "Stable" and "Unstable" stand for the stable and unstable manifold, respectively. (b) Experimental RD target patterns in absence of flow. The blue and green arrows represent the wave vector $\vec{k}$ and the vector perpendicular to the boundary $\vec{n}$, respectively. (c) Experimental reaction-diffusion-advection (RDA) structure at the lowest compression rate (8.33×10^{-3} s^{-1}). The yellow dotted lines show the frontier between the outer smeared wave zone and the inner irregular waves. The inset shows the planelike waves around the stagnation point. (d) RDA pattern at the highest compression rate (27.8×10^{-3} s^{-1}). The lines separate the outer smeared wave zone from the inner plane waves with the inset focusing on the zone around the stagnation point.

by a positive (autocatalysis) and negative (oxidation of the brominated CHD) feedback dynamics through a redox mechanism [Fig. 1(b)] [39,43,44]. The no-flux boundary condition at the rim of the reactor tends to orient the waves locally perpendicularly to the walls, i.e., with their wave vector $\vec{k}$ perpendicular to the wall normal vector $\vec{n}$. The RD pattern is characterized by the wavelength $w_b = 0.7$ mm, driven by the kinetics and diffusion, leading to a size of the black or white bands $s_c = w_b/2 = 0.35$ mm. The chemical wave speed is approximately $c = 0.11$ mm/s (see SM, Sec. II [42]).

When the hyperbolic flow is turned on ($Q \neq 0$), the injection along y and outflow along x set the preferred directions along which waves tend to align. At low Q and hence low compression rate γ [Fig. 1(c)], waves with no preferred direction develop in the central zone, in the vicinity of the stagnation point where $|\vec{v}| = 0$ (see inset). Close to the inlets and outlets where the velocity is largest, waves are smeared due to the parabolic flow profile between the two cell plates [45], and irregular patchy patterns are observed to align along flow streamlines. In the transition zone between the central irregular RD waves and the outer smeared waves, low-curvature patterns, i.e., slightly bended waves, referred to here as *planelike waves,* propagate outward [inset in Fig. 1(c); schematics shown in SM, Fig. S4 [42]]. Such planelike waves are typically observed for lower values of the compression rate (see SM, Sec. III [42]).

At higher compression rates, the waves align horizontally with a constant wavelength, i.e., with their wave vector $\vec{k}$ parallel to the $\vec{y}$ direction of the stable manifold [Fig. 1(d)]. They form a localized wave packet of finite width and zero group velocity. Within this wave packet, new waves appear close to the horizontal middle of the cell, propagate outwards along y to both sides, and disappear in the planelike wave zone, itself in contact further away with smeared waves [Fig. 1(d) and movies with explanations in SM, Sec. IV [42]].

The wave packet composed of plane waves is formed when the compression rate γ is larger than a threshold value γ_c. To determine γ_c, we initially inject the reacting solution at a low compression rate of 8.33×10^{-3} s^{-1} for more than twice the volume of the cell. Then, we increase the compression rate by steps of $\Delta\gamma = 2.8 \times 10^{-4}$ s^{-1}, up to 11.1×10^{-3} s^{-1}. The time intervals between changes in compression rate are 60 s, allowing for the flow and chemistry to stabilize every time. As the compression rate increases, the mixture of random and planelike waves present in the central part of the reactor [Fig. 1(c)] is replaced by plane waves [Fig. 1(d) and SM, Sec. III [42]). In order to characterize the transition, a middle rectangle is cropped around the stagnation point on the images and the image intensity is averaged along the x axis [Fig. 2(a)]. For the analysis of the experiments, we set that the wave packet is present in the zone where the averaged image intensity renormalized by its maximal amplitude exceeds 0.4 and features regular spatial oscillations over space and time. Figure 2(b) shows the emergence of a wave packet at $\gamma = 9.4 \times 10^{-3}$ s^{-1} and its persistence when γ is progressively increased. Space-time (ST) maps of the dynamics can be constructed by piling up the image intensity along the central line of either x or y directions. The signature of the wave packet corresponds to regular stripes on the $x - t$ map and outward propagating regular zones on the $y - t$ map [Fig. 2(d)]. This contrasts with the more irregular ST signature of planelike waves [Fig. 2(c)].

The formation of aligned plane waves in the center of the cell may be understood as a result of a competition between diffusion and compression. Under constant stretching, diffusive broadening and compression balance at the Batchelor scale $s_b = \sqrt{D/\gamma}$ [41]. Hence, diffusion dominates at scales smaller than s_b. When s_b is much larger

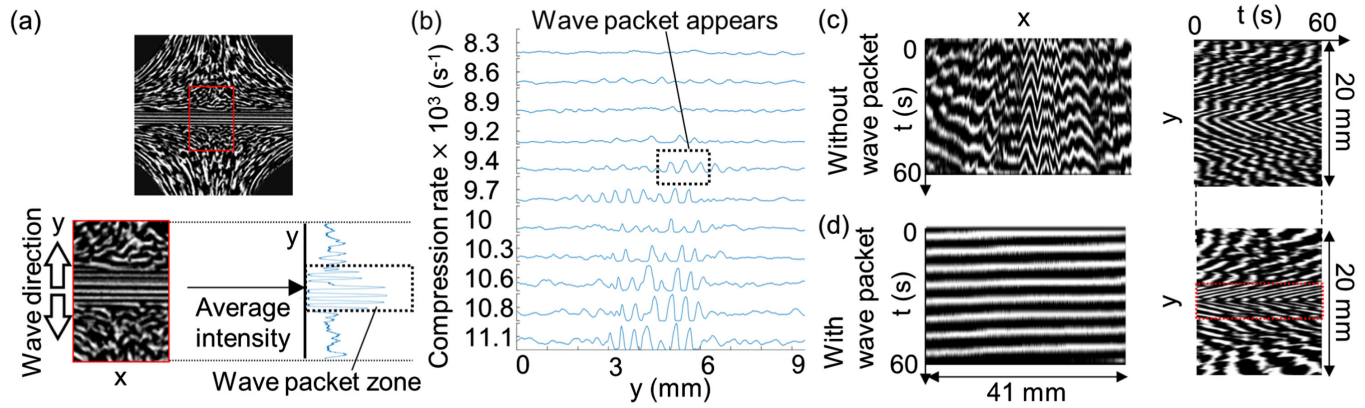

FIG. 2. (a) Image processing of the experimental pattern at $\gamma = 10.8 \times 10^{-3}$ s^{-1}. (b) Averaged image intensity as a function of y for increasing compression rates γ. (c),(d) Space-time maps of the dynamics along x (unstable manifold, left column) and y (stable manifold, right column) directions, for (c) $\gamma = 8.33 \times 10^{-3}$ s^{-1} in the absence of wave packet and (d) $\gamma = 10.8 \times 10^{-3}$ s^{-1} with wave packet (within the red dotted rectangle).

than the characteristic size s_c of the RD pattern, RD patterns with irregular waves like in Fig. 1(c) can develop by diffusion at the center of the cell. Conversely for $s_b \leq s_c$, classical RD patterns cannot form within the Batchelor scale, and the oscillator is confined at the center of the cell, with concentrations being uniform along x due to stretching. The resulting oscillations propagate outward until they get smeared by shear in the vertical direction, as discussed further below. The critical compression rate for the transition to wave packet is thus

$$\gamma_c = D/s_c^2. \tag{1}$$

Taking $D = 1.2 \times 10^{-3}$ mm^2 s^{-1} as the average diffusion coefficient of the BZ-CHD species [46] and $s_c = 0.35$ mm as estimated above in the absence of flow, we obtain $\gamma_c = 10^{-2}$ s^{-1}, which is close to the compression at the transition $\gamma = 9.4 \times 10^{-3}$ s^{-1} [Fig. 2(b)]. For $\gamma > \gamma_c$, the wave vector $\vec{k}$ of the pattern (here the planar waves) hence aligns along the direction of the compressing gradient of velocity [Fig. 1(d)].

Once a wave packet has been obtained, it imprints a privileged direction that is maintained even if the compression rate is decreased below γ_c. Starting at a large compression rate, $\gamma = 2.8 \times 10^{-2}$ s^{-1}, and decreasing γ by steps $\Delta\gamma$, the width of the wave packet increases (Fig. 3), as also observed in the average image intensity [Fig. 4(a)]. The direction of the waves can be seen on the ST maps. The (x, t) ST maps along the unstable manifold [left panels on Fig. 4(b)] show relatively straight stripes. Waves appear close to the middle of the cell and then propagate toward both sides on the (y, t) ST maps of the stable manifold [right panels on Fig. 4(b)]. Outside the undisturbed central zone of aligned plane waves [delimited by the orange

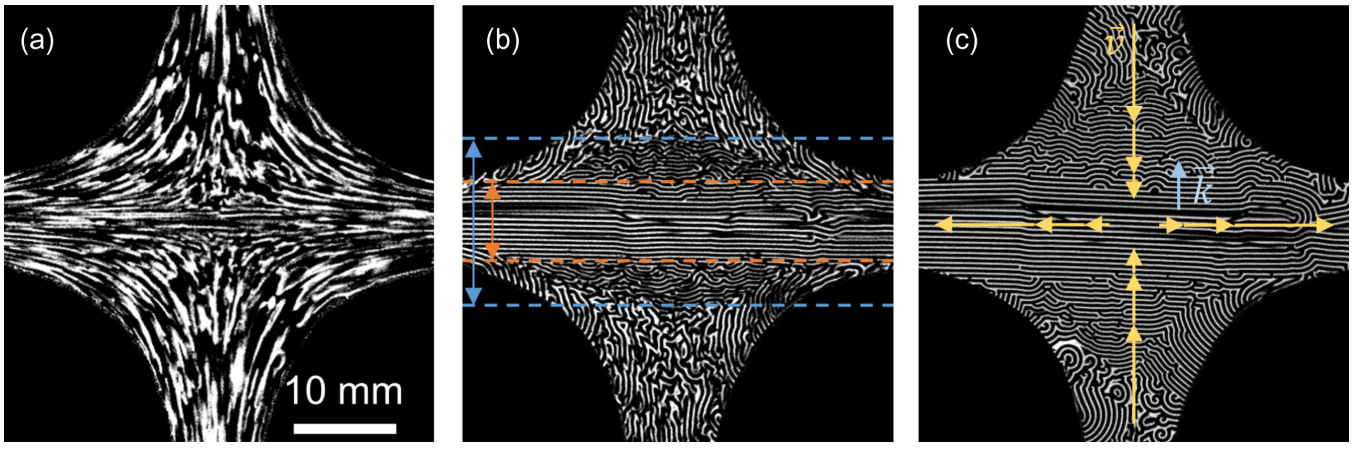

FIG. 3. Pattern formation when the compression rate is decreased stepwisely. Compression rate of (a) 8.33×10^{-3} s^{-1}; (b) 1.39×10^{-3} s^{-1}. The orange dotted lines delimitate the wave packet while the zone between the orange and blue lines encompasses the planelike waves. Smeared waves are observed outside the blue dotted lines. (c) 1.75×10^{-4} s^{-1}. The yellow arrows represent the velocity vectors $\vec{v}$ (shorter arrows represent smaller velocity); the blue arrow represents the wave vector $\vec{k}$.

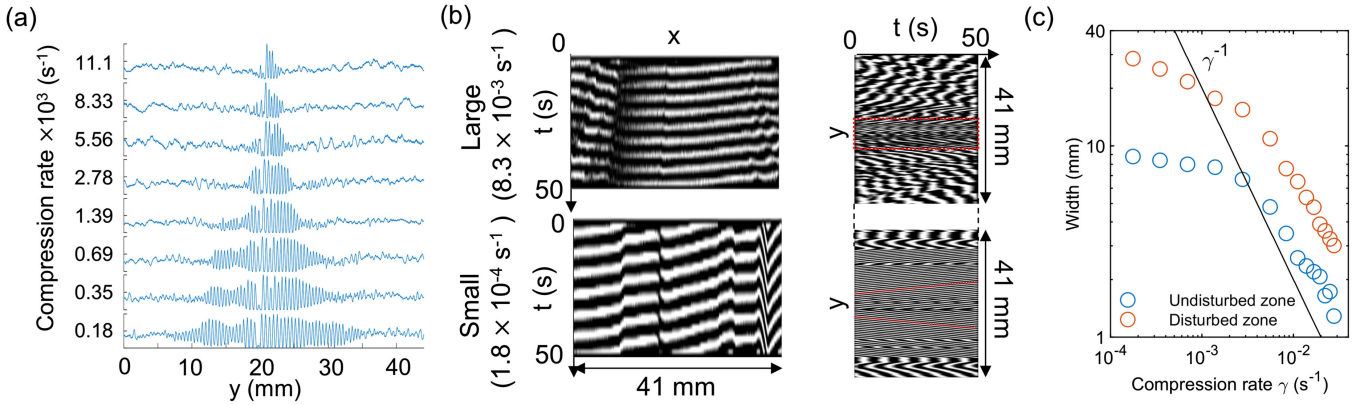

FIG. 4. (a) Average of the image intensity along y for different compression rates obtained as in Fig. 2(a). (b) S-T maps in x (unstable manifold, left panels) and y (stable manifold, right panels) directions, for large γ (8.33×10^{-3} s^{-1}; upper panels) and low γ (1.8×10^{-4} s^{-1}; lower panels). The red dotted rectangle shows the location of the wave packet. The red line in the lower right panel traces one of the traveling waves. (c) Width of the undisturbed wave zone [within orange dotted lines in Fig. 3(b)] and disturbed wave zone [within orange and blue dotted lines in Fig. 3(b)] as a function of compression rate. The solid line is the scaling γ^{-1}. See SM movies [42] for the quantification of the zone widths.

dotted lines on Fig. 3(b)], there is a disturbed zone of planelike waves with low curvatures and some defects (between the orange and blue lines) that operates the transition toward the smeared zone [outside the blue lines in Fig. 3(b)]. We measured the width of the undisturbed and disturbed wave zones as a function of γ while decreasing the compression rate. We find that these widths scale as γ^{-1} at high and intermediate γ [Fig. 4(c)]. As they approach the size of the cell, for compression rates smaller than 3×10^{-3} s^{-1}, they transit to a different regime, likely influenced by the boundary conditions [Fig. 3(c)].

In the smeared zone [region outside the blue dashed lines in Fig. 3(b)], highly irregular patterns result from the deformation of the chemical waves by the parabolic flow profile of the fluid velocity between the plates of the cell [45] (schematics in SM, Fig. S5 [42]). This deformation is significant if the y component of maximum fluid velocity of the parabolic flow profile, $v_{m,y}$, is of the order of the chemical wave speed in the stagnation zone, $c = 0.076$ mm/s, which does not vary much with γ [SM, Fig. S6(b) [42]]. The maximum velocity $v_{m,y} = 1.5\overline{v_y}$, with $\overline{v_y} = \gamma y_i$, the y component of the fluid velocity averaged over the height of the cell, is evaluated for each γ at the location y_i of the interfaces between different wave regimes [i.e., at the position y_i of the blue and orange dotted lines in Fig. 3(b)]. We find that v_m at the interface between the smeared and the disturbed wave zones is close to the average chemical wave speed at intermediate and large compression rates [Fig. S6(a) in SM [42]]. This confirms the origin of smearing at high velocities. Note that this does not hold for low compression rates as the wave zones are disturbed by the traveling waves close to the boundary [Fig. S6(a) in SM [42]]. In the central zone, the flow speed is small enough so that the deformation of the chemical wave by the parabolic profile is negligible.

We investigated the effect of fluid stretching and compression on pattern formation of the bubble-free BZ reaction-diffusion system in a hyperbolic flow imposing a constant stretching and compression rate. Increasing the compression rate, we observed a transition from random waves toward a wave packet composed of parallel plane waves above a critical compression rate γ_c. The alignment of the plane waves along the unstable manifold is obtained when compression overcomes diffusive broadening. When decreasing the compression rate starting from plane waves obtained at $\gamma > \gamma_c$, the memory of the wave packet created at large compression is sustained. Thus, a widening wave packet with a width scaling inversely to the compression rate is obtained following the imprinted pattern of the initial central wave packet. Further away, the plane waves transform into smeared waves due to the parabolic flow profile in the gap of the cell. Consistently with our experimental results, wave packets are triggered when compression is large enough to sustain a mixing scale smaller than the characteristic size of the wave pattern. Therefore, this phenomenon should occur in flows that exhibit locally or globally exponential stretching. This is particularly relevant for chaotic flows, which develop across a wide range of contexts [41,47–50]. Shear flows, such as those at the center of a vortex [51,52], produce linear stretching, which does not maintain constant mixing scales as diffusion eventually dominates over compression [53,54]. Therefore, we do not anticipate the formation of similar wave packets in such flows. Testing these hypotheses and generalizing these results to other flows should be the subject of future work. These findings underline the role of fluid stretching and compression for controlling and localizing reaction-diffusion waves under advection and pave the way to analyze the influence of a hyperbolic flow on excitable waves [10] or $A + B \rightarrow$ oscillator dynamics [28,29], for instance.

Acknowledgments—We acknowledge financial support from the ITN network CoPerMix, from Prodex and from FNRS under the CONTROL research grant.

[1] G. Nicolis and I. Prigogine, *Self-Organization in Nonequilibrium Systems* (Wiley, New York, 1977).
[2] R. Kapral and K. Showalter, *Chemical Waves and Patterns* (Springer, New York, 1995).
[3] I. R. Epstein and J. A. Pojman, *An Introduction to Nonlinear Chemical Dynamics* (Oxford University Press, New York, 1998).
[4] A. Goldbeter and M. J. Berridge, *Biochemical Oscillations and Cellular Rhythms* (Cambridge University Press, Cambridge, England, 1996).
[5] J. D. Murray, *Mathematical Biology* (Springer, New York, 2002).
[6] G. Dupont, M. Falcke, V. Kirk, and J. Sneyd, *Models of Calcium Signalling* (Springer, New York, 2016).
[7] J. Rinzel and J. B. Keller, Biophys. J. **13**, 1313 (1973).
[8] J. M. Davidenko, A. V. Pertsov, R. Salomonsz, W. Baxter, and J. Jalife, Nature (London) **355**, 349 (1992).
[9] V. Perez-Muñuzuri, R. Aliev, B. Vasiev, V. Perez-Villar, and V. I. Krinsky, Nature (London) **353**, 740 (1991).
[10] O. Steinbock, J. Schütze, and S. C. Müller, Phys. Rev. Lett. **68**, 248 (1992).
[11] A. S. Mikhailov and K. Showalter, Phys. Rep. **425**, 79 (2006).
[12] V. K. Vanag and I. R. Epstein, Chaos **18**, 026107 (2008).
[13] J. Löber and H. Engel, Phys. Rev. Lett. **112**, 148305 (2014).
[14] A. S. Zadorin, Y. Rondelez, J.-C. Galas, and A. Estevez-Torres, Phys. Rev. Lett. **114**, 068301 (2015).
[15] O. Steinbock and S. C. Müller, Phys. Rev. E **47**, 1506 (1993).
[16] C.-K. Tung and C. K. Chan, Phys. Rev. Lett. **89**, 248302 (2002).
[17] K. J. M. Bishop and B. A. Grzybowski, Phys. Rev. Lett. **97**, 128702 (2006).
[18] A. B. Rovinsky and M. Menzinger, Phys. Rev. Lett. **69**, 1193 (1992).
[19] V. N. Biktashev, A. V. Holden, M. A. Tsyganov, J. Brindley, and N. A. Hill, Phys. Rev. Lett. **81**, 2815 (1998).
[20] Z. Neufeld, Phys. Rev. Lett. **87**, 108301 (2001).
[21] V. Pérez-Muñuzuri and G. Fernández-García, Phys. Rev. E **75**, 046209 (2007).
[22] M. S. Paoletti and T. H. Solomon, Phys. Rev. E **72**, 1 (2005).
[23] J. R. Boehmer and T. H. Solomon, Europhys. Lett. **83**, 58002 (2008).
[24] J. Mahoney, D. Bargteil, M. Kingsbury, K. Mitchell, and T. Solomon, Europhys. Lett. **98**, 44005 (2012).
[25] T. D. Nevins and D. H. Kelley, Phys. Rev. Lett. **117**, 164502 (2016).
[26] M. Doan, J. J. Simons, K. Lilienthal, T. Solomon, and K. A. Mitchell, Phys. Rev. E **97**, 033111 (2018).
[27] A. von Kameke, F. Huhn, G. Fernández-García, A. P. Muñuzuri, and V. Pérez-Muñuzuri, Phys. Rev. E **81**, 066211 (2010).
[28] D. M. Escala, M. A. Budroni, J. Carballido-Landeira, A. De Wit, and A. P. Muñuzuri, J. Phys. Chem. Lett. **5**, 413 (2014).
[29] M. A. Budroni, L. Lemaigre, D. M. Escala, and A. De Wit, Langmuir **39**, 997 (2023).
[30] J.-J. Perraud, A. De Wit, E. Dulos, P. De Kepper, G. Dewel, and P. Borckmans, Phys. Rev. Lett. **71**, 1272 (1993).
[31] V. K. Vanag and I. R. Epstein, Phys. Rev. Lett. **87**, 228301 (2001).
[32] V. K. Vanag and I. R. Epstein, Phys. Rev. Lett. **88**, 088303 (2002).
[33] V. K. Vanag and I. R. Epstein, Phys. Rev. Lett. **92**, 128301 (2004).
[34] G. Haller, Annu. Rev. Fluid Mech. **47**, 137 (2015).
[35] J. J. Hidalgo, M. Dentz, Y. Cabeza, and J. Carrera, Geophys. Res. Lett. **42**, 6357 (2015).
[36] E. T. Hester, M. B. Cardenas, R. Haggerty, and S. V. Apte, Water Resour. Res. **53**, 3565 (2017).
[37] E. Bresciani, P. K. Kang, and S. Lee, Water Resour. Res. **55**, 1624 (2019).
[38] S. Izumoto, J. Heyman, J. A. Huisman, K. De Vriendt, C. Soulaine, F. Gomez, H. Tabuteau, Y. Méheust, and T. Le Borgne, Water Resour. Res. **59**, e2023WR034749 (2023).
[39] K. Kurin-Csörgei, A. M. Zhabotinsky, M. Orbán, and I. R. Epstein, J. Phys. Chem. **100**, 5393 (1996).
[40] D. M. Escala and A. P. Muñuzuri, Langmuir **35**, 13769 (2019).
[41] E. Villermaux, Annu. Rev. Fluid Mech. **51**, 245 (2019).
[42] See Supplemental Material at http://link.aps.org/supplemental/10.1103/PhysRevLett.133.218001 for movies and details on the experimental setup and results.
[43] I. Szalai and E. Körös, J. Phys. Chem. A **102**, 6892 (1998).
[44] I. Szalai, K. Kurin-Csörgei, I. R. Epstein, and M. Orbán, J. Phys. Chem. A **107**, 10074 (2003).
[45] T. D. Nevins and D. H. Kelley, J. Fluid Mech. **874**, 235 (2019).
[46] S. Anupong, I. Schreiber, and O.-U. Kheowan, Phys. Chem. Chem. Phys. **22**, 28213 (2020).
[47] H. Aref *et al.*, Rev. Mod. Phys. **89**, 025007 (2017).
[48] J. Heyman, D. R. Lester, and T. Le Borgne, Phys. Rev. Lett. **126**, 034505 (2021).
[49] J. Heyman, D. R. Lester, R. Turuban, Y. Méheust, and T. Le Borgne, Proc. Natl. Acad. Sci. U.S.A. **117**, 13359 (2020).
[50] H. Sanquer, J. Heyman, K. Hanna, and T. Le Borgne, Environ. Sci. Technol. **58**, 8899 (2024).
[51] S. Sen, P. Singh, J. Heyman, T. Le Borgne, and A. Bandopadhyay, Phys. Fluids **32**, 106602 (2020).
[52] P. Meunier and E. Villermaux, J. Fluid Mech. **476**, 213 (2003).
[53] A. Bandopadhyay, T. Le Borgne, Y. Méheust, and M. Dentz, Adv. Water Resour. **100**, 78 (2017).
[54] M. Souzy, I. Zaier, H. Lhuissier, T. Le Borgne, and B. Metzger, J. Fluid Mech. **838**, R3 (2018).